A new modeling approach of myxococcus xanthus bacteria using polarity-based reversals

Hélène Bloch, Vincent Calvez, Benoît Gaudeul, Loïc Gouarin, Aline Lefebvre-Lepot, Tam Mignot, Michèle Romanos, Jean-Baptiste Saulnier

ESAIM: PROCEEDINGS AND SURVEYS, Vol. ?, 2023, 1-10
Editors: Will be set by the publisher

A NEW MODELING APPROACH OF *MYXOCOCCUS XANTHUS* BACTERIA USING POLARITY-BASED REVERSALS *

Hélène Bloch[1], Vincent Calvez[2], Benoît Gaudeul[3], Loïc Gouarin[1], Aline Lefebvre-Lepot[1], Tam Mignot[4], Michèle Romanos[2] and Jean-Baptiste Saulnier[4]

Abstract. The aim of this paper is to model the collective behavior of *Myxococcus xanthus* bacteria to better understand the emerging patterns at the level of the colony. We use image analysis and data treatment on experimental data of *Myxococcus xanthus* bacteria as a starting point to build two models whose main novelty is the polarity-based reversals. The first model is based on contact dynamics approach and the second one follows a molecular dynamics approach. We compare the two cell-cell models and support each one with numerical simulations in 2D. The mathematical and biological aspects of each model are then discussed.

1. Introduction

Collective motion is a fascinating phenomenon that can be observed in various ways in many forms of life.

From flocking birds [31, 32] and schooling fish [29], to coordinated movements of ants and bees [30], coordinated behavior among individuals is a common feature in many systems. In this paper, we will focus on one particular system in which collective motion has been extensively studied: the bacterium *Myxococcus xanthus* (*M. xanthus*). It is known for its ability to exhibit collective behaviors such as swarming behavior, rippling, aggregation, and others. By investigating the mechanisms underlying these behaviors, we aim to gain a deeper understanding of the principles governing collective motion in this model organism and how they may be relevant to other systems.

M. xanthus is able to move by its own means, this property is called *motility*. This organism is commonly found in soil and measures a few micrometers. This bacterium is social, it interacts with its neighbors to form groups that synchronize their movements. In that case, macroscopic patterns such as rippling and swarming can be observed.

Rippling can be described as periodic and synchronous waves that correspond to thousands of cells self-organizing into bands of traveling waves in which the cells are highly aligned [26] (see Fig. 1, left part, for an example). *Swarming* is more difficult to describe because it takes on several forms (see Fig. 1, right part). When bacteria explore new areas, they establish groups that move as a single organism, and in this case, the

* *This work was supported by the European Research Council under Grant Agreement No 865711 and the French National Research Agency (ANR) through Grant ANR18-CE46-0005 (project RheoSuNN)*

[1] CMAP, CNRS, Ecole Polytechnique, I.P. Paris, 91128 Palaiseau, France

[2] Institut Camille Jordan, Université Claude Bernard, Lyon, 69100, France

[3] Université Paris-Saclay, CNRS, Laboratoire de mathématiques d'Orsay, 91405, Orsay, France

[4] Laboratoire de chimie bactérienne, 13009 Marseille, France

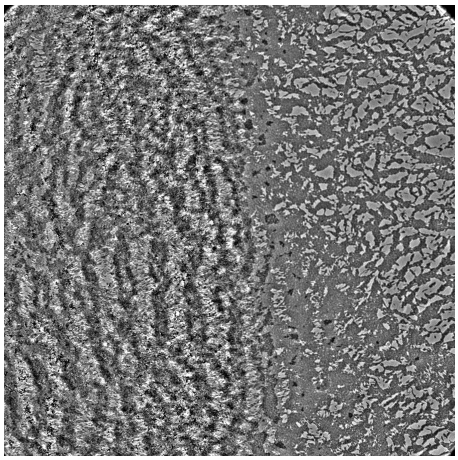

FIGURE 1. Frame taken from live movies of bacteria with 20× magnitude objective. Left: rippling (wave formation), right: swarming.

patterns formed by these groups change over time. After a certain amount of exploration, the colony begins to create a static pattern in which the cells follow specific roads. To move, these cells are equipped with a motor called the *adventurous machinery*, which allows the bacteria to propel forward and move independently [19, 20]. Movements in groups are mainly mediated by the type IV pili apparatus and are known as *social motility*. A *type IV pilus* is a growth of the bacterium that can elongate, anchor on the substrate or on other cells, and retract, allowing the bacterium to move forward [16]. These machineries are localized and assemble at a specific extremity of the bacteria. When these machineries relocate to the opposite cell pole, the bacterium rapidly changes direction of movement; this phenomenon is called a *reversal*. It has been shown that mutants (genetically engineered bacteria) that are unable to reverse do not experience rippling and produce different patterns of swarming [12, 28]. This suggests that reversals are essential for these behaviors. The cells can also secrete exopolysaccharide (EPS) proteins on the surface, and after a certain amount of time, this secretion forms a network that can be anchored by the pili of cells close to it [16]. This paper is dedicated to the development, implementation and simulation of particle-based models which can reproduce and explain swarming and rippling patterns.

To simulate rippling waves, the implementation of a refractory period (period of time during which the cell cannot reverse) seems to be crucial [5, 7, 17]. It is coupled with a sigmoid function dependent on a hypothetical signal that triggers the reversals. Biologically, this refractory period consists of the relocation time of a protein working for the reversal machinery [6]. In this case, global alignment is also required, and 1D models [5, 7, 17] are sufficient to show the emergence of rippling waves.

In the context of swarming patterns, the complexity of the models necessarily increases. Firstly, the cells are not aligned, thus a 2D model is necessary. Secondly, to see the emergence of groups of cells moving as a single organism, the implementation of contacts between cells to avoid overlap is required. In a 2015 paper, Rajesh Balagam and Oleg A. Igoshin [2] show that an additional mechanism called *slime trails following* allows to replicate patterns close to what can be observed experimentally. Note that, the dynamics of reversals are not explored, as reversals remain periodic, while experimentally, the time between reversals is far from constant. It will be discussed in Section 2.3. Our work aims to build upon the model proposed by Rajesh Balagam and Oleg A. Igoshin [2] and extend it to explore diverse reversal triggering mechanisms. We do so by adopting two approaches: the first one relies on molecular dynamics and the second one is based on contact dynamics. The novelty of both approaches lies in the polarity-based reversal mechanism which we deduced from the analysis of experimental data, see Section 2.3. Their main differences lie in the implementation of cell-cell dynamics. In the molecular dynamics approach, external forces are taken as functions of the distances between bacteria and

are chosen to avoid cell overlap Using the contact dynamics approach, intercellular forces are unknowns of the problem. Using both these approaches, we aim to better understand the underlying cellular mechanisms of the emergence of swarming patterns in *M. xanthus* bacteria.

The outline of the paper is as follows: in Section 2, we present the image and data analysis of experimental data on *M. xanthus*. In Section 3, we introduce the two mathematical models, based on the molecular dynamics approach and the contact dynamics approach. Section 4 details the implementation of the different models as well as their numerical exploration. Finally, in Section 5 we discuss our results and their relevance to pattern formation in colonies of bacteria.

2. Data analysis

In this section, we present the analysis of experimental data on *M. xanthus* bacteria, namely the velocity and reversal times of the bacteria. We explain some data acquisition techniques (image analysis and processing) as well as the result of data treatment and analysis, which will be the main pillars for the modeling of *M. xanthus* behavior, and for parameters calibration in the mathematical models.

2.1. Data acquisition and processing

To study the emergence of swarming patterns, we acquired data from the Laboratoire de Chimie Bactérienne (Marseille, France). These data consist in live segmented movies of a colony of *M. xanthus* bacteria containing roughly 1 000 bacteria in the frame of the camera. Figure 2 (left) is a zoom of Fig. 1 in the swarming part, on the right of the image. It is a frame from our dataset and showcases the segmentation process.

The variations of the light through different media allow to obtain an image with a phase contrast microscope (Fig. 2a). Segmentation (Fig. 2b is the process by which each pixel in each image of the movie (corresponding to a time frame in our case) is assigned a label. Image segmentation of bacteria movies allows us to detect the body of each bacterium, and to separate it from the background (the medium). This process gives access to the position of each bacterium at each time frame, and simplifies the representation of each bacterium to become an object defined by a sequence of points positioned along its body axis (in our case we obtain exactly nine points per bacterium, see Fig. 2c). Several algorithms for image segmentation exist, we chose the recently developed algorithm MiSiC [23] which has already given impressive results in the segmentation of bacteria colonies.

It is worth noting that the segmentation process is not perfect. Common errors can occur such as the merging of two bacteria, or defects in the process leading to a bacterium not being segmented. These defects motivate the works in Section 2.4. However, due to time constraints, we directly used the data from the process presented here.

2.2. Analysis of bacteria velocity

As the bacteria are able to travel alone, to form groups, and to travel in packs, we investigated whether the bacteria's velocity depends on the size of the group. With the segmented data at hand, we divided the bacteria into three groups: isolated bacteria, bacteria traveling in packs of two to four bacteria and bacteria traveling in swarms (very large groups moving in the same direction). We tracked each bacterium in each subgroup (in total 5 bacteria were analyzed in each subgroup type). We observed that bacteria with one or more neighbors move on average faster in the medium than isolated ones, see Fig. 3. This suggests that group size affects bacteria's velocity.

2.3. Analysis of bacteria reversal frequency

When the tracking is consistent for a sufficiently long time, several reversal events can be observed. We analyzed the reversal frequency of a given bacterium in a swarm by computing the time between two reversals. This analysis revealed a distinctive distribution of these times, bacteria had 3 min to 3.5 min between each reversal event, see Figure 4. Long times between two reversals can be underestimated because of segmentation and tracking errors, as well as the size of the field captured, and the duration of the movie. We then searched if

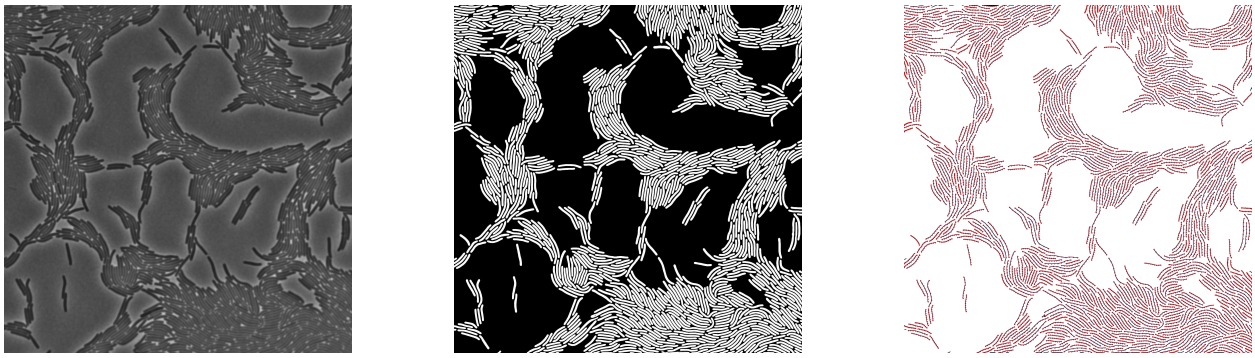

(A) Raw phase contrast snapshot of *M. xanthus* colony.

(B) Segmented image from the MiSiC software.

(C) Skeletonization of the segmented objects and detection of nine nodes (in red) along the cellular body of each bacterium.

FIGURE 2. The different steps of the segmentation process for the same image. The images are obtained using a 100× magnitude objective.

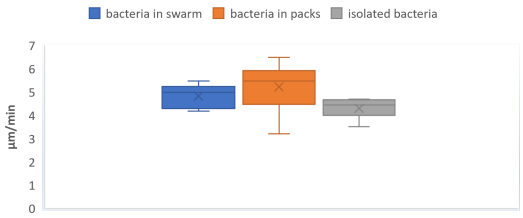

FIGURE 3. Bacteria's velocity depending on group size in three subgroups: isolated bacteria, bacteria in packs (groups of two to four bacteria), and bacteria in swarms. Mean velocity computed over 5 bacteria.

these reversal frequencies were directly correlated with either the local density or the local mean polarity. For a given cell, the local density is defined as the number of neighbors in contact with the bacterium. The local mean polarity is defined as:

$$p(i) = \begin{cases} \frac{1}{N_{c,i}} \sum_{j=1}^{N_{c,i}} \frac{\mathbf{v}_i \cdot \mathbf{v}_j}{||\mathbf{v}_i|| \, ||\mathbf{v}_j||} & \text{if } N_{c,i} >= 1 \\ 1 & \text{if } N_{c,i} = 0 \end{cases} \tag{1}$$

where i is the considered bacterium, $N_{c,i}$ is the number of cells in contact with the bacterium i, and with a slight abuse of notation $\mathbf{v}_i$ and $\mathbf{v}_j$ are the speed of the bacterium and its j-th neighbor, respectively.

Figures 4 and 5 show the local density and polarity as functions of the size of the group. We compared the distribution of time between reversals for a low density (resp. polarity) of bacteria and for a high density (resp. polarity). Our analysis first showed that there is no link between the local density and the frequency of reversals (see Fig. 4). It revealed on the other hand that more frequent reversals might be linked to (or triggered by) a bacterium facing groups of opposite orientations (see Fig. 5), as we obtain a significantly lower mean of times between reversals for bacteria with low polarity.

2.4. **Trajectory smoothing**

Experimental data on *M. xanthus* suggest that reversals occur at rest. During the segmentation process, incorrect merges of two bacteria might occur. Therefore, the center of mass of a cell can be moved by a large factor between two frames. We present here a method to deal with this issue.

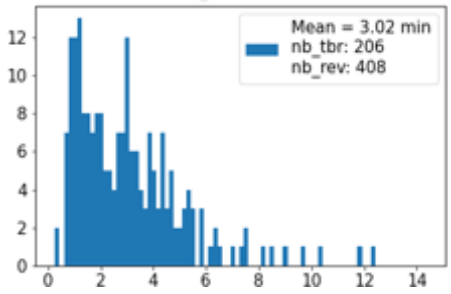

(A) Three or less immediate neighbors.

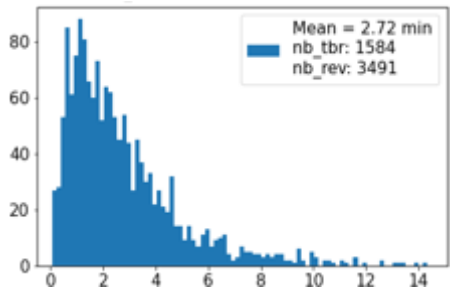

(B) More than three immediate neighbors.

FIGURE 4. Number of reversals as a function of time for a given bacterium with different number of neighbors.

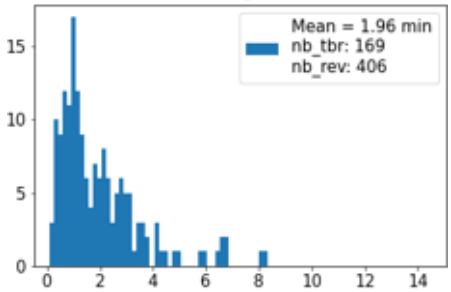

(A) Negative polarity.

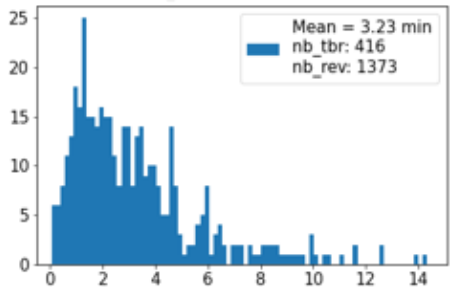

(B) Positive polarity.

FIGURE 5. Number of reversals as a function of time for a given bacterium with different polarity.

To look more closely at the speed of the bacteria around reversals, we need a sub-pixel precision on the position of the bacteria. To achieve this precision, we assume that the trajectories of the center of mass are continuous and piecewise Bézier curves of degree three. A Bézier curve of degree three is parametrized by four points $\mathbf{A}, \mathbf{B}, \mathbf{C}, \mathbf{D}$ of $\mathbb{R}^2$.

It refers both to the following function

$$\begin{array}{ccc} [0,1] & \to & \mathbb{R}^2 \\ t & \mapsto & (1-t)^3\mathbf{A} + 3t(1-t)^2\mathbf{B} + 3t^2(1-t)\mathbf{C} + t^3\mathbf{D}, \end{array}$$

and the set of its images.

Since the continuity part in *piecewise continuous Bézier curve* is equivalent to setting the first point $\mathbf{A}$ of a piece as the last one $\mathbf{D}$ of the previous piece. To account for the sharp changes of direction, we chose not to enforce a higher regularity. This sets the support of the trajectory.

To be able to measure the speed of a cell, we need to set the speed at which this trajectory is traveled. For each section, we let $t_{\text{wait},i} \geq 0$ the time spent at the beginning of the trajectory and $v_i > 0$, such that the Bézier curve is described in a time $\frac{1}{v_i}$. Formally given k sections parametrized by $i \in [\![1, k]\!]$ and $(\mathbf{A}_i, \mathbf{B}_i, \mathbf{C}_i, \mathbf{D}_i)$, (t_i), and (v_i) the associated degrees of freedom, we let,

$$T_i = \sum_{l=1}^{i-1} t_{\text{wait},l} + \frac{1}{v_l} \qquad \text{and} \qquad j(t) = \sup\left\{i \in [\![1,k]\!] | T_i \leq t\right\},$$

respectively the time spent before section i and the section associated with the current time $t \in [0,1]$. Using these functions, we introduce:

$$\mathbf{P}(t) = \mathbf{P}_{j(t)}\left(\frac{t - T_{j(t)} - t_{\text{wait},j(t)}}{v_j}\right),$$

where

$$\mathbf{P}_j(t) = \begin{cases} \mathbf{A}_j & \text{if } t < 0, \\ (1-t)^3\mathbf{A}_j + 3t(1-t)^2\mathbf{B}_j + 3t^2(1-t)\mathbf{C}_j + t^3\mathbf{D}_j & \text{if } 0 \le t \le 1, \\ D_j & \text{if } t > 1 \text{ and } j = k, \end{cases}$$

and for $j \in [\![2,k]\!]$ we have $\mathbf{A}_j = \mathbf{D}_{j-1}$. In other words, we have to choose $3k+1$ points and $2k$ real numbers. These degrees of freedom are then fitted to the measurements using a cost function. To account for rare but large errors in the dataset, instead of the usual Euclidean distance squared d^2, we took $\frac{d^2}{1+\frac{d^2}{1000}}$. The dataset contains positions in pixels and times in frame numbers. Formally given $(\mathbf{M}_i, f_i)$ said positions and times, the degrees of freedom are set to minimize:

$$\text{cost}_{\mathbf{M},f} : \mathbf{A}_1, (\mathbf{B}_j, \mathbf{C}_j, \mathbf{D}_j)_{j\in[\![1,k]\!]}, (t_{\text{wait},j})_{j\in[\![1,k]\!]}, (v_j)_{j\in[\![1,k]\!]} \mapsto \sum_i \frac{|| \mathbf{P}(f_i) - \mathbf{M}_i ||^2}{1 + \frac{||\mathbf{P}(f_i) - \mathbf{M}_i||^2}{1000}}.$$

In other words, we want our smoothed trajectory to be as close as possible of the measured one in a time-space sense and not only spatially. This process could be improved in several ways. As shown in Fig. 6, the degrees of freedom t_i does not seem to be useful, and the positions of the breaks are difficult to obtain.

Considering only the center of mass may seem simplistic since the data set provides eight additional points. We attempted to take them into account in the equation by adding an elastic cost to the objective function, however the added complexity made the optimization problem much harder and thus the code too slow to be usable (data not shown).

The choice of parametrization made has the advantage of simplicity. However, the strong coupling between speed and position felt somewhat unnatural, therefore we attempted to choose it independently. Here again we were unable to reliably solve the optimization problem.

Improving the initial guess for the optimization problem could solve the issues mentioned previously.

We could also use higher order Bézier curves to detect the reversals more accurately and automatically.

3. Mathematical modeling of collective movement of *M. xanthus*

3.1. **Modeling of bacteria**

Inspired by Balagam and Igoshin [2], we model a bacterium as a string of disks moving on a plane. The disks forming a cell stay permanently in contact, either punctually or with a fixed overlap. We call the centers of these disks *nodes*. As discussed in the introduction, a model in dimension at least two is required. In our dataset, cells do not overlap, therefore, a 3D model is not necessary.

Let us write N the number of disks in a bacterium and r their radius. For the sake of simplicity, we assume that every disk has the same radius, even for two different bacteria.

We present a model that is continuous in time and space, the discretization of this system will be discussed in Section 4.2.

Let us consider M bacteria. For $i \in [\![1,M]\!]$ and $j \in [\![1,N]\!]$, let us write $\mathbf{p}_{i,j}$ the position of the center of the j-th disk of the bacterium i. For $i' \in [\![1,M]\!]$ and $j' \in [\![1,N]\!]$, we denote by $d_{i,j}^{i',j'} = || \mathbf{p}_{i,j} - \mathbf{p}_{i',j'} || - 2r$ the signed distance between the disk j in the bacterium i and the disk j' in the bacterium i'. Bacteria i and i' can be different. Two bacteria should not overlap, i.e., $d_{i,j}^{i',j'} \ge 0$ for two disks that are not consecutive in a bacterium (see Fig. 7). Furthermore, we impose $d_{i,j}^{i,j+1} \le 0$ so two disks in a bacterium stay in contact.

M. xanthus is rod-shaped, that is it resembles Fig. 8a. Our modeling choice does not include this geometry directly. To obtain a closer version of the rod shape, we can allow two consecutive disks to overlap. The

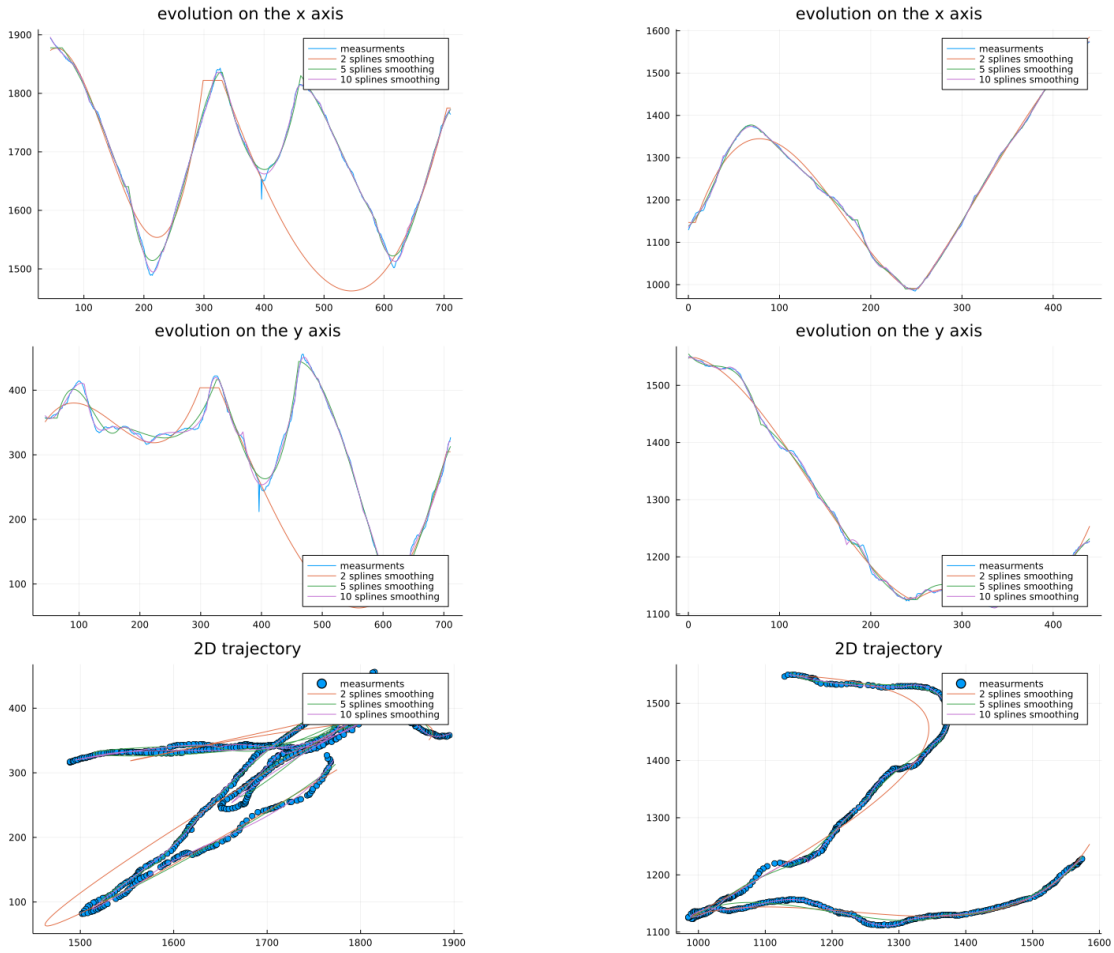

FIGURE 6. Smoothing of the trajectory for two bacteria.

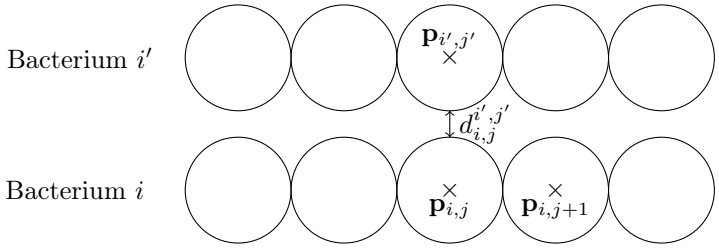

FIGURE 7. Notations for contacts.

condition $d_{i,j}^{i,j+1} = 0$ is replaced by $d_{i,j}^{i,j+1} = -\varepsilon$ with $0 \leq \varepsilon \leq r$. With $\varepsilon = 0$, we recover the initial case (Fig. 8d). On the other hand, $\varepsilon = r$ leads to the configuration represented by Fig. 8b, but prevents the bacterium to bend. Figure 8c shows a bacterium with $\varepsilon \in (0, r)$. The cell can still bend, which is closer to the physical behavior of a bacterium.

Swarming patterns are characterized by groups of cells that move in packs with minimal superposition. To replicate such patterns in our simulations, it is essential to implement contact mechanisms between the cells

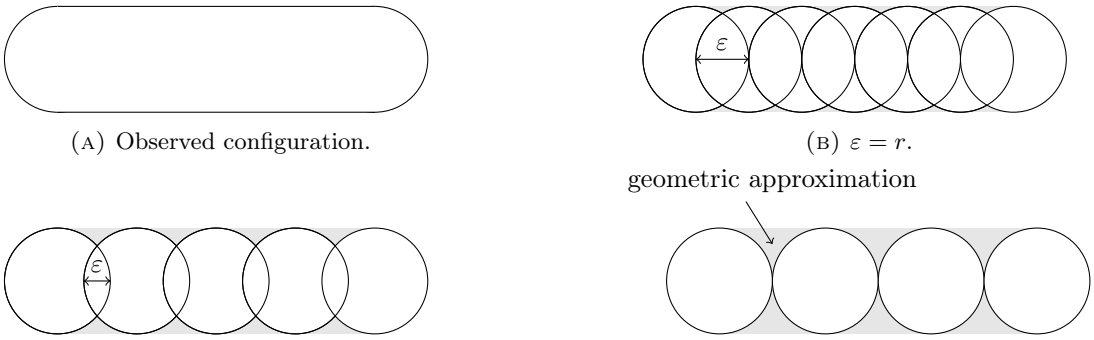

(A) Observed configuration. (B) $\varepsilon = r$. (C) $\varepsilon \in (0; r)$. (D) $\varepsilon = 0$.

FIGURE 8. Modeled bacteria with different values of ε.

which we detail in what follows. Formally, the positions $\mathbf{p}_{i,j}$, $i \in [\![1, M]\!]$, $j \in [\![1, N]\!]$ are assumed to be solutions of the following *ordinary differential equation* (ODE)

$$\frac{d}{dt}\mathbf{p}_{i,j} = \mathbf{v}_{\mathrm{n}i,j} + \sum_{(i',j') \text{ such that } d_{i,j}^{i',j'} \leq r_c} \mathbf{v}_{\mathrm{c}i,j}^{i',j'} + \mathbf{v}_{\mathrm{e}i,j}, \tag{2}$$

where $\mathbf{v}_{\mathrm{n}i,j}$ represents the natural motion of a bacterium. It is the velocity a bacterium "wants" to have, without taking the presence of other bacteria into account. Choices for $\mathbf{v}_{\mathrm{n}i,j}$ are discussed in Section 3.2. The force denoted by $\mathbf{v}_{\mathrm{c}i,j}^{i',j'}$ is a *contact force* such that disks are subject to the conditions $d_{i,j}^{i,j+1} = -\varepsilon$ for two consecutive disks in a bacterium and $d_{i,j}^{i',j'} \geq 0$ for other disks. Several choices are discussed in Section 3.3. Finally, $\mathbf{v}_{\mathrm{e}i,j}$ represents the external force applied on disk j in the bacterium i. This force can be written as the sum of forces by the disk j' in the bacterium i' and by the external medium where bacteria are moving. Then we have:

$$\mathbf{v}_{\mathrm{e}i,j} = \sum_{(i',j') \text{ such that } d_{i,j}^{i',j'} \leq r_c} \mathbf{v}_{\mathrm{e}i,j}^{i',j'} + \mathbf{v}_{\mathrm{e}i,j}^{\mathrm{EPS}}$$

We discuss the use of these forces to model the rigidity of a bacterium in Section 3.5 and the modeling of type IV pili in Section 3.6. The cut-off radius r_c is explained in Section 4.2.1.

Remark 1. *Note that our model is a first order ODE and therefore does not encompass inertia. The aforementioned terms denoted by $\mathbf{v}_{c_{i,j}}^{i',j'}$ and $\mathbf{v}_{e_{i,j}}$ are in fact correction terms for the velocity. Referring to these terms as "forces" is justified by the fact that this system can be seen as the limit of a mechanical viscous model of order two. For the remainder of this paper, we refer to these terms either as "forces" or as "velocity-correcting terms".*

3.2. **Natural motion of a bacterium**

To describe the motion of an isolated bacterium i, we developed and implemented four models. All of them rely on a parameter v representing the norm of the speed of the bacterium which can be fixed using the analysis done in Section 2.2. We also introduce the vectors $\mathbf{e}_{i,j}^{-} = \frac{\mathbf{p}_{i,j-1} - \mathbf{p}_{i,j}}{||\mathbf{p}_{i,j-1} - \mathbf{p}_{i,j}||}$ and $\mathbf{e}_{i,j}^{+} = \frac{\mathbf{p}_{i,j+1} - \mathbf{p}_{i,j}}{||\mathbf{p}_{i,j+1} - \mathbf{p}_{i,j}||}$. Let us notice that $\mathbf{e}_{i,j+1}^{-} = -\mathbf{e}_{i,j}^{+}$.

In the first model, we assume that the bacterium is a rigid non-rotating body so that we have, for all nodes j, $\mathbf{v}_{\mathrm{n}i,j} = \mathbf{v}_{\mathrm{n}i,1}$. We also set $\mathbf{v}_{\mathrm{n}i,1} = v\mathbf{e}_{i,2}^{-}$. We named this model *parallel* due to the orientation of the velocities.

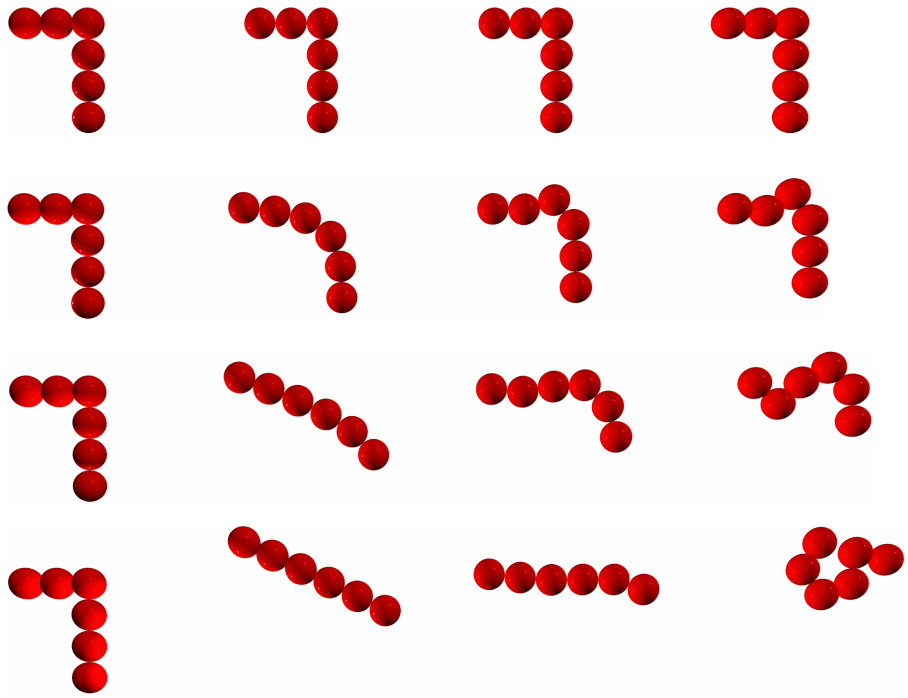

FIGURE 9. Trajectory of non-straight bacterium moving to the left. From top to bottom with parallel, towed, pulled, and pushed mobility. From left to right at adimentionnal times 0, 5, 15, 30.

In the second model, we also want the speed to be v, however, we assume that only the head (the first disk in the string) participates in the motion of the bacterium thus $\mathbf{v}_{\mathrm{n}i,1} = Nv\mathbf{e}^-_{i,2}$ and $\mathbf{v}_{\mathrm{n}i,j} = \mathbf{0}$ for $j \in [\![2, N]\!]$. This model could be accurate for a pili-driven motility, we will refer to it as *towed*.

The last two models are somewhat similar in their conception. They are respectively called *pulled* and *pushed*. For both of them we have $\mathbf{v}_{\mathrm{n}i,1} = v\mathbf{e}^-_{i,2}$ and $\mathbf{v}_{\mathrm{n}i,N} = v\mathbf{e}^-_{i,N}$ the difference lies in the inner nodes:

$$\mathbf{v}_{\mathrm{n}i,j} = \begin{cases} v\mathbf{e}^-_{i,j} \text{ pulled,} \\ -v\mathbf{e}^+_{i,j} \text{ pushed,} \end{cases}$$

so that as their names indicate the nodes are either pulled by the one in front of them or pushed by the one behind them. A convex combination of these models could be used to model the autonomous motility of *M. xanthus*.

As one can notice from Fig. 9 the pushed model does not yield realistic results, but we include it for symmetry purposes and to allow linear combinations of the models. We discuss this idea in Section 5. We note here that the 3D visual effect of disks in Fig. 9 is only a choice of visualization. All computations are performed on a plane.

3.3. **Treatment of contacts**

To complete the description of *M. xanthus*, we still need to model the contacts between bacteria. We explored two different methods.

In Section 3.3.1, we use a contact dynamics approach where the velocity-correcting terms $\mathbf{v}_{\mathrm{c}i,j}^{i',j'}$ (see Remark 1) are unknowns of the problems. They are deduced from Lagrange multipliers associated to the constraint on

$d_{i,j}^{i',j'}$. A second method is discussed in Section 3.3.2 based on a molecular dynamics approach. In the latter, the velocity-correcting terms $\mathbf{v}_{\mathrm{c}i,j}^{i',j'}$ are given by an explicitly computable formula such as Hook's law. Nevertheless, the forces can be stiff, which can be challenging to treat numerically.

These two methods enable us to investigate the effect of different contact models on the emergence and stability of swarming patterns.

3.3.1. *Contact dynamics approach*

This method has been developed in several articles [10, 11, 21, 22] to study the motion of rigid mechanical particles. In this method, the contact forces are not functions of the distance. They are proportional to the Lagrange multiplier associated to the constraint on the distance. In the continuous model, if the initial condition does not satisfy the constraints, the contact forces are no longer functions of the time but may include Dirac masses. The implicit scheme used to approximate them in Section 4.2 is still naturally well defined in most of these pathological conditions.For sake of readability we will not attempt to expend our continuous definition to these edge cases.

This method is typically is used to impose a positive distance between two particles. In [8], it has been extended to particles that stay in contact. We shall consider two cases:

- if the two disks are consecutive in a bacterium, we impose $d_{i,j}^{i,j'} = -\varepsilon$ for $i \in [\![1, M]\!]$, $j \in [\![1, N]\!]$ and $j' = j - 1$ (if $j \neq 1$) or $j' = j + 1$ (if $j \neq N$);
- otherwise, we impose $d_{i,j}^{i',j'} \geq 0$ for $i, i' \in [\![1, M]\!]$, $j, j' \in [\![1, N]\!]$, and in the special case $i' = i$, then we have $j' \notin [\![j - 1, j + 1]\!]$.

To stay in the framework of contacts dynamics, the first condition writes,

$$d_{i,j}^{i',j'} \geq -\varepsilon \text{ and } d_{i,j}^{i',j'} \leq -\varepsilon.$$

The implementation of this method is detailed in Section 4.1.1

3.3.2. *Molecular dynamics approach*

Unlike the model described in Section 3.3.1, the contact forces have an explicit formulation in the molecular dynamics approach. As explained previously, we model a bacterium as a succession of disks at a constant distance between each other. We first focus on the enforcement of this constraint, then we introduce a repulsive force between each disk to prevent overlaps. We use the Hooke's law to impose $d_{i,j}^{i,j\pm1} = -\varepsilon$ for two consecutive nodes and a quadratic force to have $d_{i,j}^{i',j'} \geq 0$ for other nodes.

The Hooke's law to control the distance between disks. Enforcing a constant distance requires a force that acts as a repulsive force if the nodes are too close, and an attractive force if they are too for away. To that extent, we model the contact force as a spring with high stiffness between each consecutive node of a bacterium. This yields the following force:

$$\mathbf{v}_{\mathrm{c}i,j}^{i,j+1} = k_s(d_{i,j}^{i,j+1} + \varepsilon)\mathbf{e}_{i,j}^{+} \qquad \text{and} \qquad \mathbf{v}_{\mathrm{c}i,j}^{i,j-1} = k_s(d_{i,j}^{i,j-1} + \varepsilon)\mathbf{e}_{i,j}^{-}$$

where k_s is the stiffness constant of the springs.

Repulsion between disks. To avoid overlap between non-consecutive disks we apply a repulsive force between each disk j and another disk close enough j'. The same force is applied whether the two disks belong to the same bacterium or not, as long as they are not consecutive in a single bacterium ($j' \notin [\![j - 1, j + 1]\!]$ if the two disks belong to the same bacterium). This repulsive force is quadratic to avoid too strong repulsion in case of a small overlap while preventing large overlaps. Formally, we set:

$$\mathbf{v}_{\mathrm{c}i,j}^{i',j'} = -k_{\mathrm{r}} \left(\min \left(d_{i,j}^{i',j'},\ 0 \right) \right)^2 \mathbf{e}_{i,j}^{i',j'},$$

where k_r is the "magnitude" of the repulsive force and $\mathbf{e}_{i,j}^{i',j'}$ is the normalized vector pointing from the position $\mathbf{p}_{i,j}$ to the position $\mathbf{p}_{i',j'}$, $\mathbf{e}_{i,j}^{i',j'} = \frac{\mathbf{p}_{i',j'}-\mathbf{p}_{i,j}}{||\mathbf{p}_{i',j'}-\mathbf{p}_{i,j}||}$. The choice of a squared distance allows for C^1 regularity in the formulation of the forces, while the minimum ensures that the force acts only for overlapping objects. We recall that the repulsive force between a disk and both itself and its adjacent neighbors coming from the same chain of disks are set to 0.

3.4. **Reversal mechanisms**

We tested three different reversal mechanisms to understand how these mechanisms are linked to the swarming patterns. We first tested if it can emerge without any reversals. Then, based on biological data suggesting the presence of an internal clock governing the bacteria's reversal [6], we considered this possibility by conferring asynchronous reversal clocks to the bacteria colony. Upon reaching its intrinsic clock period, the bacterium reverses its axis. Finally, as our data analysis (Section 2.3) revealed a link between the surrounding polarity of each bacterium and the reversal frequencies, we tested if this reversal mechanism can induce the swarming pattern. The bacterium i reverses its axis if it is facing more oppositely-directed bacteria than bacteria with the same direction as its own, i.e., if $p(i) < 0$, where the polarity p has been defined in Section 2.3. Our last model encompasses features from the other two. It is a stochastic model past a refractory time t_ref follows a memory-less law whose parameter λ depends on the polarity. Formally between times t and $t + \Delta t$ the reversal probability of a bacterium i is $\lambda_i \Delta t + o(\Delta t)$. The term λ_i can be computed using the time since the last reversal of the bacterium $t_{c,i}$, the refractory time t_ref, a dimensionless parameter w representing the willingness to reverse, and the polarity p_i which has been defined by Eq. (1) of Section 2.3.

$$\lambda_i = \begin{cases} 0 & \text{if } t_{c,i} < t_\mathrm{ref} \\ 1 - \exp(-w\frac{1-p_i}{2}) & \text{otherwise} \end{cases}$$

3.5. **Stiffness of a bacterium**

The mathematical modeling of a bacterium as an ideal string of disks allows motions that are not observed in experiments, especially when bacteria bend. To tackle this issue, we use external forces to model the stiffness of a cell. First, we consider a model commonly used [8, 9], then show that this model does not preserve the inter-center distances and thus required additional contact forces to be consistent with the framework presented in previous section. A second model, derived from a gradient-flow, is introduced to remedy this issue. Finally, we discuss the relative merits of each model.

The first model is given by angular springs supplemented with Newton's third law of motion. Given a bacterium i and $j \in [\![2, N-1]\!]$ an inner disk, we let $R = 2r - \varepsilon$ the distance between $\mathbf{p}_{i,j-1}$ and $\mathbf{p}_{i,j}$. As previously stated, this is also the distance between any two nodes and in particular, $\mathbf{p}_{i,j}$ and $\mathbf{p}_{i,j+1}$. We add the following forces:

$$\begin{aligned} \mathbf{v}_{\mathrm{e}_{i,j-1}}^{i,j} &= -\frac{k}{R}\left(\mathbf{e}_{i,j}^{+} - \left(\mathbf{e}_{i,j}^{-}\cdot\mathbf{e}_{i,j}^{+}\right)\mathbf{e}_{i,j}^{-}\right) && \text{on disk } j-1 \\ \mathbf{v}_{\mathrm{e}_{i,j+1}}^{i,j} &= -\frac{k}{R}\left(\mathbf{e}_{i,j}^{-} - \left(\mathbf{e}_{i,j}^{-}\cdot\mathbf{e}_{i,j}^{+}\right)\mathbf{e}_{i,j}^{+}\right) && \text{on disk } j+1 \\ \mathbf{v}_{\mathrm{e}_{i,j}}^{i,j} &= -\mathbf{v}_{\mathrm{e}_{i,j-1}}^{i,j} - \mathbf{v}_{\mathrm{e}_{i,j+1}}^{i,j} && \text{on disk } j, \end{aligned} \tag{3}$$

where k is a constant representing the stiffness of a bacterium. As shown in Fig. 10, the forces $\mathbf{v}_{\mathrm{e}_{i,j-1}}^{i,j}$ and $\mathbf{v}_{\mathrm{e}_{i,j+1}}^{i,j}$ are orthogonal to $\mathbf{e}_{i,j}^{-}$ and $\mathbf{e}_{i,j}^{+}$ respectively. This is intuitively consistent to what one would expect from a stiffness model, however, since the force on the middle node is not zero (to preserve Newton's third law of motion), the inter-center distances are not preserved. This can be clearly seen in Figs. 11a to 11c for a three disks long bacterium.

To remedy this issue, we also derive an L^2 gradient-flow of the discrete curvature energy: $\sum_j \frac{||\mathbf{e}_{i,j}^{+}+\mathbf{e}_{i,j}^{-}||^2}{2R}$ associated with the constraint $d_{i,j}^{i,j\pm1} = -\varepsilon$ [24]. To compare the models, we provide explicit computations for

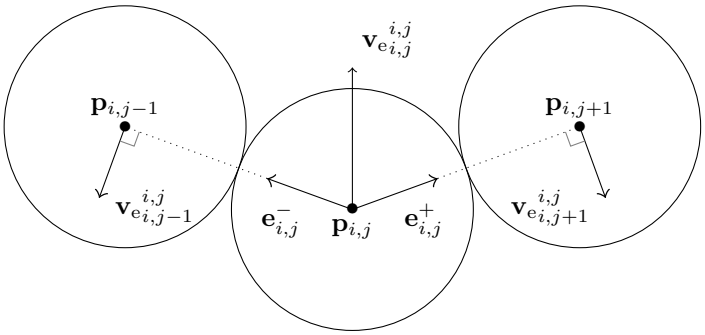

FIGURE 10. Notations and forces at play with model Eq. (3) for bacterium i.

a three disks long bacterium (Figs. 11d to 11f). The derivative of the energy, and therefore the forces (up to a negative multiplicative constant) is:

$$\begin{pmatrix} 2\left(\mathbf{e}_{i,2}^{+}+\mathbf{e}_{i,2}^{-}\right)+\pi_{1,2}\mathbf{e}_{i,2}^{-} \\ -4\left(\mathbf{e}_{i,2}^{+}+\mathbf{e}_{i,2}^{-}\right)-\pi_{1,2}\mathbf{e}_{i,2}^{-}-\pi_{3,2}\mathbf{e}_{i,2}^{+} \\ 2\left(\mathbf{e}_{i,2}^{+}+\mathbf{e}_{i,2}^{-}\right)+\pi_{3,2}\mathbf{e}_{i,2}^{+}, \end{pmatrix}$$

where $\pi_{1,2}$ and $\pi_{3,2}$ are the Lagrange multiplier associated with the constraints $d_{i,1}^{i,2}=-\varepsilon$ and $d_{i,3}^{i,2}=-\varepsilon$, respectively. To find the values of $\pi_{1,2}$ and $\pi_{3,2}$, we notice that:

$$\left(\frac{d}{dt}\mathbf{p}_{i,1}-\frac{d}{dt}\mathbf{p}_{i,2}\right)\cdot\mathbf{e}_{i,2}^{-}=0 \text{ and } \left(\frac{d}{dt}\mathbf{p}_{i,3}-\frac{d}{dt}\mathbf{p}_{i,2}\right)\cdot\mathbf{e}_{i,2}^{+}=0,$$

so that:

$$\pi_{1,2}=\pi_{3,2}=-6\frac{\mathbf{e}_{i,2}^{+}\cdot\mathbf{e}_{i,2}^{-}+1}{\mathbf{e}_{i,2}^{+}\cdot\mathbf{e}_{i,2}^{-}+2}.$$

To be able to compare the models we can fix the proportionality constant such that for shallow angles, both models behave similarly:

$$\begin{aligned}
\mathbf{v}_{\mathrm{e}_{i,1}}^{i,2} &= -\frac{k}{R}\left(\mathbf{e}_{i,2}^{+}-\frac{2\mathbf{e}_{i,2}^{+}\cdot\mathbf{e}_{i,2}^{-}+1}{\mathbf{e}_{i,2}^{+}\cdot\mathbf{e}_{i,2}^{-}+2}\mathbf{e}_{i,2}^{-}\right)\\
\mathbf{v}_{\mathrm{e}_{i,3}}^{i,2} &= -\frac{k}{R}\left(\mathbf{e}_{i,2}^{-}-\frac{2\mathbf{e}_{i,2}^{+}\cdot\mathbf{e}_{i,2}^{-}+1}{\mathbf{e}_{i,2}^{+}\cdot\mathbf{e}_{i,2}^{-}+2}\mathbf{e}_{i,2}^{+}\right)\\
\mathbf{v}_{\mathrm{e}_{i,2}}^{i,2} &= -\mathbf{v}_{\mathrm{e}_{i,1}}^{i,2}-\mathbf{v}_{\mathrm{e}_{i,3}}^{i,2}.
\end{aligned}$$

Although the gradient-flow model has interesting properties, its implementation is very challenging since it requires explicit computations for each length of bacteria N in the simulation. Moreover, adding implicit contact forces, that is the smallest (in L^2) perturbation of the forces given by the first model that satisfies the constraint, we conjecture that for bacterium that do not cross themselves we obtain the gradient-flow model as emphasized by Fig. 12.For the sake of simplicity and due to the independent implementation of contact forces, we maintain Eq. (3) when accounting for the stiffness.

3.6. **Type IV pili modeling**

M. xanthus bacteria use type IV pili machinery located on their leading pole to move. These pili can elongate, anchor to extracellular polymeric substances (EPS) or to other bacteria, and retract to propel the cell

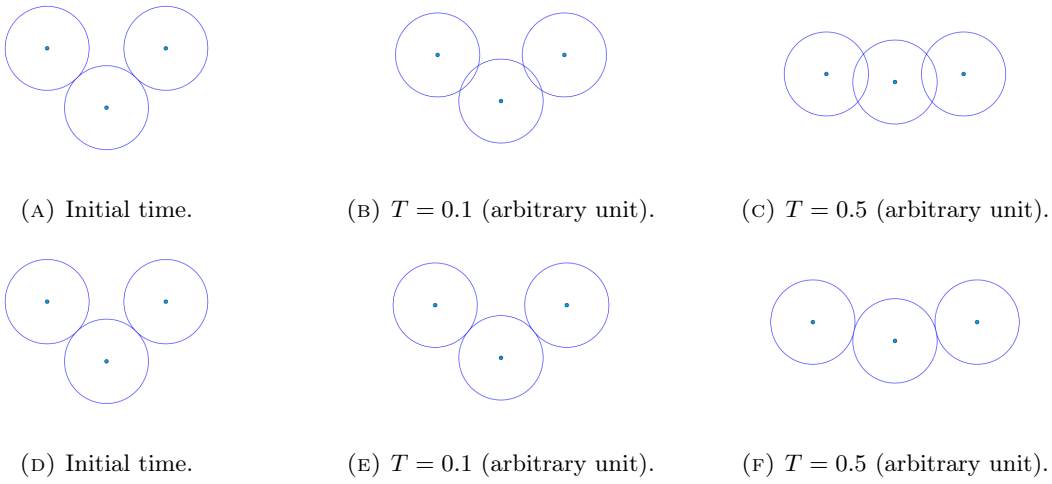

(A) Initial time. (B) $T = 0.1$ (arbitrary unit). (C) $T = 0.5$ (arbitrary unit).

(D) Initial time. (E) $T = 0.1$ (arbitrary unit). (F) $T = 0.5$ (arbitrary unit).

FIGURE 11. Stiffness-driven evolution of a three disk bacterium. Top, angular springs model. Bottom, gradient flow-model.

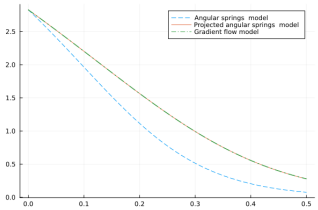

FIGURE 12. Evolution of curvature energy with time.

forward [16]. Experiments with mutants lacking this machinery show a decrease in group size and coordinated motion [19, 33].

In the following sections, we describe how we model the type IV pili mechanism. First we define the region reached by the pili, then model independently the attraction with other bacteria and the EPS.

3.6.1. *Pili search area*

We suppose that *M. xanthus* can elongate its pili only in the forward direction. More precisely, the bacterium i can "see" (i.e, detect neighbors) with an angle of view $2\alpha_i$, $\alpha_i \in [0, \frac{\pi}{2}]$, in front of it and a horizon $H_i > 2r$. Let us recall that $\mathbf{e}_{i,2}^-$ is the direction of said head so that the area of the plane viewed by the bacterium is formally given by:

$$S_i = \left\{ \mathbf{x} \in \mathbb{R}^2 \middle| \exists l \in (0, H_i], \theta \in [-\alpha_i, \alpha_i], \mathbf{x} = \mathbf{p}_{i,1} + lQ(\theta)\mathbf{e}_{i,2}^- \right\},$$

where $Q(\theta) = \begin{pmatrix} \cos(\theta) & \sin(\theta) \\ -\sin(\theta) & \cos(\theta) \end{pmatrix}$ is the rotation matrix of angle θ.

3.6.2. *Attraction with neighbors*

Given that the pili are localized at the cell pole, we added an attraction force on the head of each bacterium. This attraction force is defined as being in the direction of the head to the closest node of another bacterium in its field of view S_i. Let i', $(i' \neq i)$ and j' be the label of this other bacteria and node respectively. If the other bacteria are too far away, the attraction force is set to zero. Otherwise, the strength of said attraction force is a function of the distance between the two bacteria, as illustrated by Fig. 13. This function is continuous,

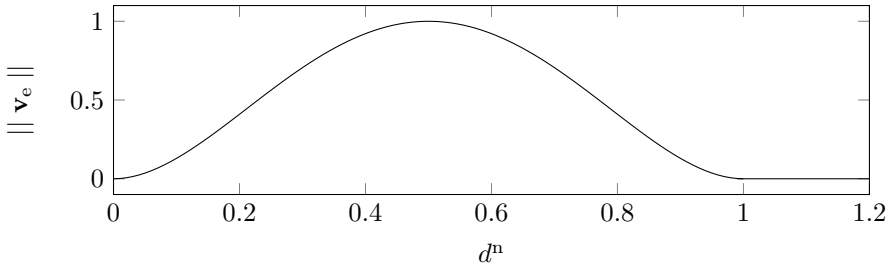

FIGURE 13. Attraction force as a function of the distance between two bacteria.

polynomial by part and equal to zero if the bacteria are in contact or too far away. It is given by the following formula:

$$\mathbf{v}_{\mathrm{e}}{}_{i,1}^{i',j'} = -k_a d^{\mathrm{n}}(d^{\mathrm{n}}-1)(4+(d^{\mathrm{n}}-1/2)(8-16d^{\mathrm{n}}))\ \mathbf{e}_{i,1}^{i',j'},$$

where d^{n} is obtained from the distance with the closest neighbor $\mathbf{p}_{i',j'}$ using $d^{\mathrm{n}} = \min\left(\max\left(\frac{d_{i,1}^{i',j'}}{H_i - 2r}, 0\right), 1\right)$. Notice that we do not enforce Newton's third law of motion and leave the attracting node unchanged. This models the stronger bound with the substrate in the middle of a bacterium.

3.6.3. *Slime trail following*

In this section we focus on the modeling of the EPS using a slime trail following, as Balagam and Igoshin [2]. In this model, each bacterium deposits a certain amount of EPS during its displacement which evaporates with a rate λ. To avoid feedback-loops, the EPS is deposited by the tail node of the bacterium only. The force induced by the EPS models a nematic alignment with the point of highest concentrations, provided it reaches a sufficient threshold. If the threshold is not met, the force is set to zero. If it is met, the force does not depend on the value of this concentration but only on the angle between the direction of the bacterium and the point of highest concentration.

Implementation details are provided in Section 4.2.2.

4. Implementation and numerical simulations

4.1. **Numerical schemes**

We use a standard discretization in time, with a fixed time step Δt, and we write $t^n = n\Delta t$, with $n \in \mathbb{N}$. For both codes, the speed and external forces are discretized explicitly, however the contact forces are implemented implicitly for the contact dynamics approach and with a Lie splitting [27] in the molecular dynamics case.

4.1.1. *Numerical scheme for contact dynamics*

As explained previously, with the contact dynamics approach, contact forces are unknowns of the problem, thus we need to treat them with an implicit scheme. Formally we set:

$$\mathbf{p}_{i,j}^{n+1} = \mathbf{p}_{i,j}^{n} + \Delta t \mathbf{v}_{\mathrm{n}}{}_{i,j}^{\mathrm{base},n} + \Delta t \sum_{(i',j') \text{ such that } d_{i,j}^{i',j',n} \leq r_c} \mathbf{v}_{\mathrm{c}}{}_{i,j}^{i',j',n+1} + \Delta t \sum_{(i',j') \text{ such that } d_{i,j}^{i',j',n} \leq r_c} \mathbf{v}_{\mathrm{e}}{}_{i,j}^{i',j',n}, \qquad (4)$$

where the superscript n (resp. $n+1$) indicates that we approximate the value of the corresponding object at time t^n (resp. t^{n+1}). The parameter r_c is a cut-off radius used for performance purposes. In fact, the two velocity-correcting terms $\mathbf{v}_{\mathrm{c}}{}_{i,j}^{i',j'}$ and $\mathbf{v}_{\mathrm{e}}{}_{i,j}^{i',j'}$ are equal to zero for particles far enough. Let us notice that we do not discuss the external forces applied by the external medium $\mathbf{v}_{\mathrm{e}}{}_{i,j}^{\mathrm{EPS}}$.

This model can be written as the resolution of a convex optimization problem under constraint at each time step:

$$\min_{\mathbf{v}^{n+1}\in K^{n+1}} J\left(\mathbf{v}^{n+1}\right), \tag{5}$$

with

- with a slight abuse of notation, $\mathbf{v}^{n+1} \in \mathbb{R}^{NM}$ refers to both the variable and the solution of this convex problem; it is a vector that contains the velocities of all nodes in all bacteria at time t^{n+1};
- $J(\mathbf{v}) = \frac{1}{2}||\mathbf{v}-\mathbf{V}^{n+1}||$, where $\mathbf{V}^{n+1}$ is the *free flight velocity* given by $\mathbf{V}^{n+1} = \mathbf{v}^n + {\mathbf{v}_\mathrm{e}}^n$, where ${\mathbf{v}_\mathrm{e}}^n \in \mathbb{R}^{NM}$ is a vector that contains the resulting (or sum of) external forces applied to all nodes in all bacteria.
- K^{n+1} is the set of admissible velocities; it is made of affine inequality constraints for each disk.

From [14], $\mathbf{v}^{n+1}$ is the projection of $\mathbf{V}^{n+1}$ on K^{n+1}. We then let:

$$\mathbf{p}_{i,j}^{n+1} = \mathbf{p}_{i,j}^n + \Delta t \mathbf{v}^{n+1}.$$

At each time step, an optimization problem has to be solved. There exists several methods, such as gradient-like methods [18] or primal-dual interior-point algorithm [1, 4, 13, 25].

Further details about the derivation of Eq. (5) can be found in [14]. This model is implemented in the code SCoPI developed at CMAP laboratory [15].

Solving a convex optimization problem at each time step is costly, thus we attempt to keep a large time step. Numerous algorithms based on iterative methods exist and which are not discussed here. To ensure convergence, we restrict the value of Δt with a rule of thumbs, such that a node is moved at most of 30% of its radius at each time step.

4.1.2. *Numerical scheme for molecular dynamics*

Since the contact forces are very stiff to ensure small penetrations, a very small value of Δt should be used. Computing all the forces for such a small time step would be very costly, therefore a Lie splitting is implemented. Formally we let $\tilde{\mathbf{p}}_{i,j}^n$ encompass the forces defined previously except for the contact forces based on Hook's law: ${\mathbf{v}_\mathrm{c}}_{i,j}^{i,j-1}$ and ${\mathbf{v}_\mathrm{c}}_{i,j}^{i,j+1}$ which require a finer time step and the EPS which requires a grid search:

$$\tilde{\mathbf{p}}_{i,j}^n = \mathbf{p}_{i,j}^n + \Delta t {\mathbf{v}_\mathrm{n}}_{i,j}^{\mathrm{base},n} + \Delta t \sum_{(i',j') \text{ such that } d_{i,j}^{i',j',n} \leq r_c} {\mathbf{v}_\mathrm{e}}_{i,j}^{i',j',n} + \Delta t \sum_{(i',j') \text{ such that } d_{i,j}^{i',j',n} \leq r_c \text{and} (i',j') \neq (i,j\pm 1)} {\mathbf{v}_\mathrm{c}}_{i,j}^{i',j',n},$$

then compute:

$$\tilde{\mathbf{p}}_{i,j}^{n+\frac{k+1}{N_t}} = \tilde{\mathbf{p}}_{i,j}^{n+\frac{k}{N_t}} + \frac{\Delta t}{N_t}\left({\mathbf{v}_\mathrm{c}}_{i,j}^{i,j-1,n,k} + {\mathbf{v}_\mathrm{c}}_{i,j}^{i,j+1,n,k}\right),$$

where N_t is a fixed number of subcycles and $k \in [\![0, N_t - 1]\!]$. Finally, we let:

$$\mathbf{p}_{i,j}^{n+1} = \tilde{\mathbf{p}}_{i,j}^{n+1} + \Delta t {\mathbf{v}_\mathrm{e}}_{i,j}^{\mathrm{EPS},n},$$

where ${\mathbf{v}_\mathrm{e}}_{i,j}^{\mathrm{EPS},n}$ is set to zero for $j \neq 1$ and will be detailed in Section 4.2.2.

It can be seen as an approximate solution of the optimization problem presented above, however it comes from a different modeling approach. Notice that, for performance purposes the bacteria interacting with each-other are not re-computed in the contact dynamics step, which differs from the classical Lie-splitting.

4.2. **Implementation**

The two modeling approaches described previously, that is, the contacts dynamics approach and the molecular dynamics approach, were implemented in two different codes, each corresponding to one of the two methods described in Section 3.3 to treat inter-bacteria contacts.

The contact dynamics approach (Section 3.3.1) is implemented in the code SCoPI. This code is designed for the simulation of interacting particles. It is written in C++ and uses multithreaded libraries to be executed in a high performance computing (HPC) context. We implemented the string of disks model, as well as the different motions described in Section 3.2, the stiffness model (Section 3.5), the different reversion models (Section 3.4), and the attraction with neighborhood model (Section 3.6.2). The simulations with SCoPI were performed in an infinite medium.

The molecular dynamics approach (Section 3.3.2) was implemented in a code written in Python. The models implemented in SCoPI were also implemented in this code and the type IV pili model described in Section 3.6.3 was added. The simulations performed with the Python code were carried out in a periodic domain.

4.2.1. *Detection of neighbors*

We must detect the neighbors of all disks, either to build the matrix of constraints in the contact dynamics model, or to compute the forces applied on the disk in the molecular dynamics approach. Several choices of implementation can be done. In SCoPI, a dynamic list is updated at each time step. In the Python code, we search for the K neighbors of each bacterium (so that each bacterium has exactly K neighbors), with K chosen large enough so that all bacteria in a given radius are considered as neighbors. We then use a cut-off radius r_c so that only cells inside this radius are considered as the bacterium's effective neighbors [1] with which forces will be exchanged.

For performance reasons, both codes use kd-trees to determine the closest neighbors, such as the one implemented by the libraries nanoflann [3] or SciPy spatial algorithms.

4.2.2. *Implementation of the slime trail following*

We now exhibit the details of the implementation of the slime trail following in the Python code. For the positions of the nodes we used a grid-less approach. Keeping this principle to deal with EPS deposits is overly costly since it would require to keep in memory the history of all bacteria. Therefore, we introduce a Cartesian grid $\Gamma = \Delta x \mathbb{Z}^2$. This grid can then either be truncated or stored sparsely. For any point $\mathbf{x} \in \Gamma$ we denote by $c(\mathbf{x})$ the amount of EPS present at this point.

At each time step, and for each bacterium, a normalized quantity 1 is added to $c(\mathbf{x}_i)$, where $\mathbf{x}_i \in \Gamma$ is the grid point closest to $\mathbf{p}_{i,N}$ the last node or tail of the bacterium. Once each bacterium has deposited EPS, the value on the grid c is multiplied by $\exp(-\lambda \Delta t)$ to account for the evaporation. The slime trail impacts the trajectory of a bacterium i when it is present in sufficient quantity $c_{\min}$ at a grid point in the cell's field of view S_i, where S_i was defined in Section 3.6. In this case, we let $\mathbf{x}_{\mathrm{EPS},i} = \arg\max_{\mathbf{x} \in S_i \cap \Gamma} c(\mathbf{x})$ be the grid point with the highest value in S_i, $\mathbf{e}_{\mathrm{EPS},i} = \frac{\mathbf{x}_{\mathrm{EPS},i} - \mathbf{p}_{i,1}}{||\mathbf{x}_{\mathrm{EPS},i} - \mathbf{p}_{i,1}||}$ the unit vector pointing to this point, and $\mathbf{e}_{i,2}^{-\perp}$ be a unit vector orthogonal to $\mathbf{e}_{i,2}^{-}$.

Using these notations a force is applied on the head node:

$$\mathbf{v}_{\mathrm{e}i,1}^{\mathrm{EPS}} = \gamma (\mathbf{e}_{\mathrm{EPS},i} \cdot \mathbf{e}_{i,2}^{-\perp})\, \mathbf{e}_{i,2}^{-\perp},$$

where $\gamma > 0$ models the attraction strength. This force tends to change the direction of the head toward the highest concentration of EPS (nematic alignment) with speed γ without changing the value of the speed of the bacterium. This modeling feature has been implemented in the Python code.

4.2.3. *Diversity of bacteria*

In the biological experiments on *M. xanthus* (Fig. 1), the length and the width of cells may vary. In SCoPI, we allow bacteria to have a different number of nodes. The description in Section 3.3.1 can be easily extended to this case. Similarly, two different bacteria may be modeled with a different radius r. However, we impose that two nodes in the same bacterium have the same radius. In the Python code, bacteria have the same number of nodes with identical radius.

[1] Even if a bacterium is isolated, it will have the same number of K detected neighbors as a bacterium surrounded by other cells. However, it will have no effective neighbors in the considered radius r_c and the resulting forces exchanged are equal to zero.

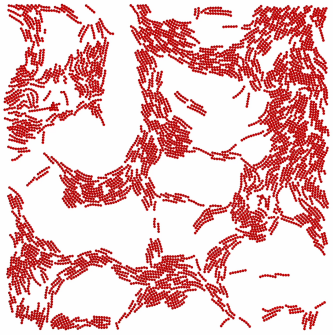

FIGURE 14. Numerical simulation in SCoPI: initial condition.

Parameter	Value
Cut-off radius (r_c)	$4r$
Velocity of the bacteria (v)	3 µm min^{-1}
Overlap between disks (ε)	0
Angle view (2α)	π
Horizon search (H)	$4r$
Stiffness of angular springs (k)	1 µm^2 min^{-1}
Magnitude of the pili attraction (k_a)	1 µm min^{-1}

TABLE 1. Numerical parameters used in simulations with SCoPI.

(A) Absence of reversals. (B) Clock-based reversal mechanism. (C) Polarity-based reversal mechanism.

FIGURE 15. Numerical simulation in SCoPI at $t_f = 50$ min.

4.3. **Numerical results**

4.3.1. *Contacts dynamics in an unbounded domain*

With the modeling framework described previously, we conducted three numerical simulations. Each one incorporates one of the following reversal mechanisms: none, clock-based, and polarity-based. Our first goal is to investigate whether this modeling framework can maintain a swarming pattern if it is initially imposed.

Parameters. The three simulations share the following parameters. The initial condition is taken from the experimental data (namely from the frame presented in Fig. 2). The bacteria distribution is identical to a time frame in the live movie where the swarming pattern occurs, see Fig. 14.

The radius and the number of disks in a bacterium are inherited from the time frame considered. Values of other parameters are given by Table 1.

Results. In Fig. 15a, we show the final configuration of the simulation at time $t_f = 50$ min in the absence of reversals. Very large packs of aligned bacteria are formed and travel together (mainly continuously rotating in the same direction). One can also note the absence of swarming patterns. As open boundary conditions are used, the loss of the initial bacteria density is expected. This may contribute to the absence of swarms which require congestion. Isolated bacteria become more scarce throughout the simulation as they join larger groups and travel with them. These patterns were observed in mutant bacteria which have lost the ability to reverse [2].

We then considered initially asynchronous clock-based reversals with a period of $t_f = 1$ min, see Fig. 15b. Although open boundary conditions are used allowing bacteria to exit the represented numerical frame, the periodic reversals allow to keep a constant average density. Large packs are able to establish but disintegrate soon after their formation due to the reversals. This result was expected as the reversal mechanism in this case

is specific to each bacterium and pertains to its own internal clock, without considering the collective behavior of surrounding bacteria. The swarms are thus unable to form in this case due to the rapid disintegration of packs, allowing for the appearance of isolated bacteria.

Finally, we look at the polarity-based reversal mechanism in Fig. 15c. Here again, we lose the initial bacteria density due to repetitive reversals. The remaining bacteria either travel in large packs or are isolated, and the swarming pattern is lost very fast by the disintegration of packs.

Altogether, our results recapitulate some behaviors observed in bacteria colonies and reveal the importance of maintaining congestion for the emergence of swarming patterns.

4.3.2. *Molecular dynamics and type IV pili*

In this section we present the simulations performed with the Python code. We use periodic boundary conditions to keep the bacteria density constant during the entire simulation. We investigate the effect of three features: type IV pili attraction, slime trail following, and polarity-based reversals (defined in Sections 3.4 and 3.6). The velocity and size of each bacterium are constant and respectively equal to 4 µm min^{-1} and 5 µm (measured from our dataset, see Fig. 3).

All simulations start with a random position and direction for each bacterium (Fig. 16a). We generate five simulations to understand the role of each feature: one simulation without any feature (Fig. 16b), three simulations testing each feature independently (Figs. 16c to 16e), and one simulation with all three features (Fig. 16f). We use the towed motion (defined in Section 3.2) to generate movement, and we do not implement the force defined in 3.5. This differs from the previous section where the pull motion is used. The model parameters can be found in Table 2.

For the reversals, we used the stochastic model presented in Section 3.4. It is both polarity and clock based. Figure 16d shows the result when using this reversal feature and without any head attraction nor slime trail following. Surprisingly, compared to the simulation obtained in Section 4.3.1, the size of the groups does not differ much compared to the simulation without reversals (Fig. 16b).

However, the attraction due to the action of the pili clearly shows an increase in the size of the groups (Fig. 16c). The search area and the distance of interaction of the pili are defined in Section 3.6.

The slime trail following constrains each bacterium to stay inside the most explored space. After one hour of simulation, a large proportion of the bacteria are trapped inside a large road at the center of the space due to the slime trail's attraction (Fig. 16e). The slime trails are colored in black, and many of them are empty as they are connected to the big slime trail at the center of the space. Bacteria moving on the smaller slime trails are trapped in the center of the domain and cannot escape.

The Fig. 16f is the combination of all the features. In this case, we observe a greater diversity of the slime trail, compared to Fig. 16e, due to the addition of reversals and pili attraction.

In Fig. 17, we can see two different patterns of swarming of *M. xanthus* observed in experiments. The left panel of the figure shows patterns that are similar to those observed in Figs. 16b to 16d. The simulation recapitulates very well the cell behavior in the experimental data where cells explore all the space uniformly over time. The right panel, in which certain areas are never visited (simulation video not included in the data shown here), shows similar behavior to what we observe in Fig. 16f with the slime trail following feature. These patterns arise from the observation of *M. xanthus* colonies, but the specific conditions that give rise to such patterns are currently unknown.

5. Discussion and conclusion

In this paper, we presented two mathematical models in the spirit of [2] and whose main novelty is the polarity-based reversal mechanism of *M. xanthus* bacteria. We brought to light this mechanism using image and data analysis of biological experiments on *M. xanthus* bacteria. The first model follows a contact dynamics approach. It is implemented using SCoPI. The second model uses a molecular dynamics approach. It is based on attractive-repulsive distance-dependent forces to treat the cell-cell contacts. This model is implemented in Python and is additionally endowed with the slime trail following mechanism. Let us notice that the implementation of the

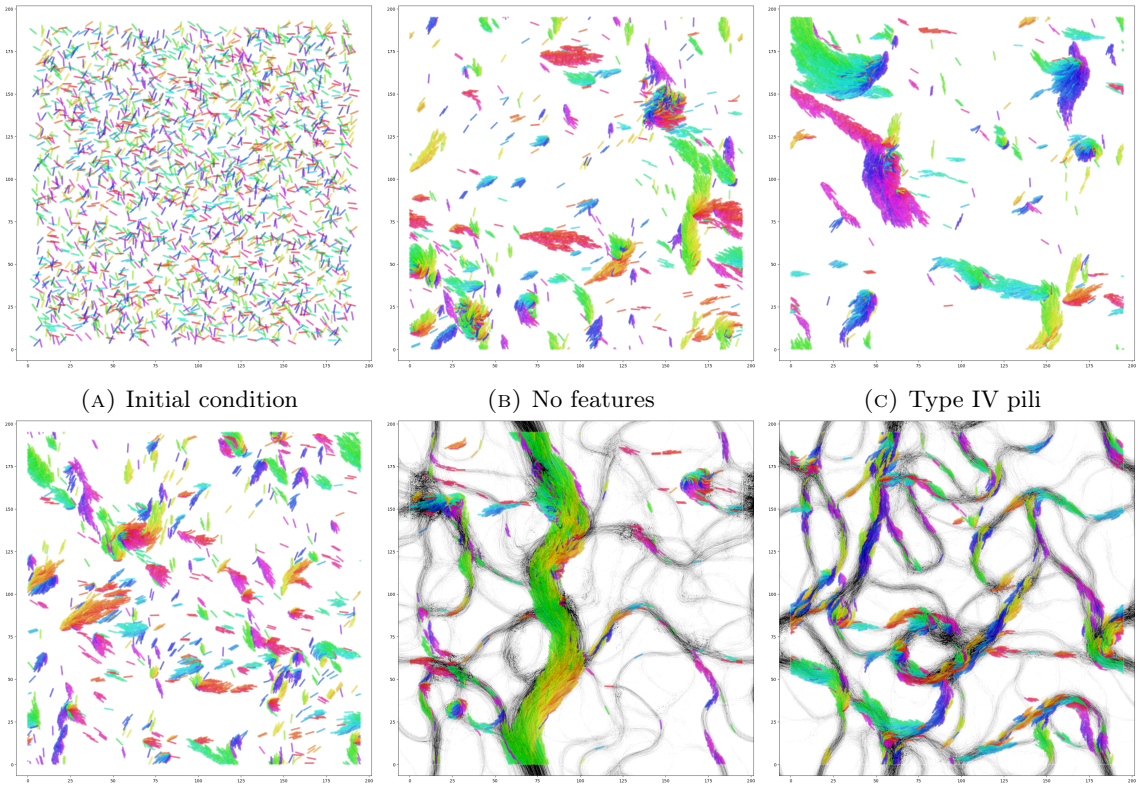

(A) Initial condition (B) No features (C) Type IV pili

(D) Polarity-based reversals with refractory period (E) Slime trail following (F) All features

FIGURE 16. Results of the numerical simulations in Python after 60 min. Bacteria are colored depending on the direction of their head.

slime trail following model was not achieved in SCoPI due to time constraints and is left for future works. Our numerical simulations in SCoPI first reveal the importance of appropriate boundary conditions in the contact dynamics approach. Considering periodic boundary conditions will keep the initial density constant throughout the numerical simulations, which allows for constant high congestion. The periodic boundary conditions were used in the molecular dynamics simulations and clearly show the persistence of cell congestion. The drawback in the molecular approach is the necessity to fine-tune the attractive-repulsive forces to be able to reproduce the observed dynamics. This tuning is rather difficult as the experimental data on hand do not allow us to do so. On the other hand, although the cell motility mechanisms are sufficient to reproduce the bacteria motility observed in the experimental data, both models could make use of combining different motility mechanisms. For example, we could endow the bacteria with the ability to alternate its motility between the towed and the pulled motilities depending on its environment. This is motivated by the fact that in the presence of neighboring bacteria, the pili are the main drivers of cell motility (towed), whereas when isolated, cells move using the pulled mechanism on the substrate. In a future work, we want to implement the EPS deposit and run simulations using periodic boundary conditions with SCoPI.

Overall, our image analysis as well as our numerical simulations reveal a novel reversal mechanism to the literature based on cell polarity, which can explain the emerging patterns at the colony level.

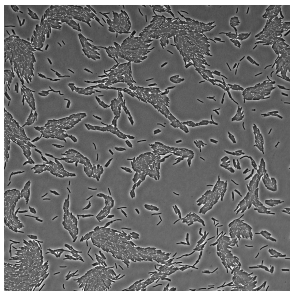

(A) Cell pattern leaving no empty spaces.

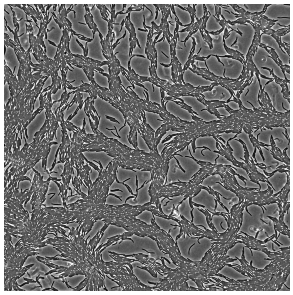

(B) Cell pattern leaving empty spaces.

FIGURE 17. Phase contrast images of the *M. xanthus* colony taken with 100× magnification objective.

Parameter	Value
Size of the space	195 µm
Number of bacteria (M)	2 700
Number of disks per bacterium (N)	10
Radius of the disks (r)	0.7 µm
Velocity of the bacteria (v)	4 µm min^{-1}
Overlap between disks (ε)	0.2 µm
Hooke's spring constant (k_s)	50 min^{-1}
Magnitude of the repulsion (k_r)	400 μm^{-1} min^{-1}
Angle view (2α)	π
Horizon search (H)	3.75 µm
Magnitude of the pili attraction (k_a)	1.5 µm min^{-1}
EPS attraction strength (γ)	6 µm min^{-1}
EPS evaporation rate (λ)	$\frac{1}{12}$ min^{-1}
Minimal EPS value detectable (c_{min})	0.1
Refractory time (t_{ref})	5 min
Willingness to reverse (w)	2

TABLE 2. Numerical parameters used in simulations with Python.

REFERENCES

[1] M. Andersen, J. Dahl, Z. Liu, L. Vandenberghe, S Sra, S Nowozin, and SJ Wright. Interior-point methods for large-scale cone programming. *Optimization for machine learning*, 5583, 2011.

[2] Rajesh Balagam and Oleg A Igoshin. Mechanism for collective cell alignment in myxococcus xanthus bacteria. *PLoS computational biology*, 11(8):e1004474, 2015.

[3] Jose Luis Blanco and Pranjal Kumar Rai. nanoflann: a C++ header-only fork of FLANN, a library for nearest neighbor (NN) with kd-trees. `https://github.com/jlblancoc/nanoflann`, 2014.

[4] E. Corona, D. Gorsich, P. Jayakumar, and S. Veerapaneni. Tensor train accelerated solvers for nonsmooth rigid body dynamics. *Applied Mechanics Reviews*, 71(5), 2019.

[5] Pierre Degond, Angelika Manhart, and Hui Yu. An age-structured continuum model for myxobacteria. *Mathematical Models and Methods in Applied Sciences*, 28(09):1737–1770, 2018.

[6] Mathilde Guzzo, Seán M Murray, Eugénie Martineau, Sébastien Lhospice, Grégory Baronian, Laetitia My, Yong Zhang, Leon Espinosa, Renaud Vincentelli, Benjamin P Bratton, et al. A gated relaxation oscillator mediated by frzx controls morphogenetic movements in myxococcus xanthus. *Nature microbiology*, 3(8):948–959, 2018.

[7] Oleg A Igoshin, Alex Mogilner, Roy D Welch, Dale Kaiser, and George Oster. Pattern formation and traveling waves in myxobacteria: theory and modeling. *Proceedings of the National Academy of Sciences*, 98(26):14913–14918, 2001.

[8] Mourad Ismail and Aline Lefebvre-Lepot. A Necklace Model for Vesicles Simulations in 2D. *International Journal for Numerical Methods in Fluids*, 76(11):835–854, December 2014.

[9] Albertas Janulevicius, Mark CM van Loosdrecht, Angelo Simone, and Cristian Picioreanu. Cell flexibility affects the alignment of model myxobacteria. *Biophysical journal*, 99(10):3129–3138, 2010.

[10] M. Jean. The non-smooth contact dynamics method. *Computer Methods in Applied Mechanics and Engineering*, 177(3):235–257, 1999.

[11] M. Jean and J. J. Moreau. Unilaterality and dry friction in the dynamics of rigid body collections. In *1st Contact Mechanics International Symposium*, pages 31–48, Lausanne, Switzerland, 1992.

[12] Lars Jelsbak and Lotte Søgaard-Andersen. Pattern formation: fruiting body morphogenesis in myxococcus xanthus. *Current Opinion in Microbiology*, 3(6):637–642, 2000.

[13] K. Krabbenhoft, A. V. Lyamin, J. Huang, and M. Vicente da Silva. Granular contact dynamics using mathematical programming methods. *Computers and Geotechnics*, 43:165–176, 2012.
[14] Aline Lefebvre. Numerical simulation of gluey particles. *ESAIM: Mathematical Modelling and Numerical Analysis - Modélisation Mathématique et Analyse Numérique*, 43(1):53–80, 2009.
[15] A. Lefebvre-Lepot. `SCoPIwebpage,http://www.cmap.polytechnique.fr/~lefebvre/SCoPI/index.html`, 2022.
[16] Yinuo Li, Hong Sun, Xiaoyuan Ma, Ann Lu, Renate Lux, David Zusman, and Wenyuan Shi. Extracellular polysaccharides mediate pilus retraction during social motility of myxococcus xanthus. *Proceedings of the National Academy of Sciences*, 100(9):5443–5448, 2003.
[17] Angelika Manhart. Counter-propagating waves in a system of transport-reaction equations. *arXiv preprint arXiv:1801.06869*, 2018.
[18] H. Mazhar, T. Heyn, D. Negrut, and A. Tasora. Using nesterov's method to accelerate multibody dynamics with friction and contact. *ACM Transactions on Graphics (TOG)*, 34(3):1–14, 2015.
[19] T Mignot. The elusive engine in myxococcus xanthus gliding motility. *Cellular and Molecular Life Sciences*, 64:2733–2745, 2007.
[20] Tâm Mignot, Joshua W Shaevitz, Patricia L Hartzell, and David R Zusman. Evidence that focal adhesion complexes power bacterial gliding motility. *Science*, 315(5813):853–856, 2007.
[21] J.J. Moreau. Unilateral Contact and Dry Friction in Finite Freedom Dynamics. In J.J. Moreau and P.D. Panagiotopoulos, editors, *Nonsmooth Mechanics and Applications*, International Centre for Mechanical Sciences, pages 1–82. Springer, Vienna, 1988.
[22] J.J. Moreau. Numerical aspects of the sweeping process. *Computer Methods in Applied Mechanics and Engineering*, 177(3-4):329–349, 1999.
[23] Swapnesh Panigrahi, Dorothée Murat, Antoine Le Gall, Eugénie Martineau, Kelly Goldlust, Jean-Bernard Fiche, Sara Rombouts, Marcelo Nöllmann, Leon Espinosa, and Tâm Mignot. Misic, a general deep learning-based method for the high-throughput cell segmentation of complex bacterial communities. *eLife*, 10:e65151, sep 2021.
[24] M. A. Peletier. Variational modelling: Energies, gradient flows, and large deviations. Lecture Notes, Würzburg. Available at `http://www.win.tue.nl/∼mpeletie`, Feb. 2014.
[25] C. Petra, B. Gavrea, M. Anitescu, and F. Potra. A computational study of the use of an optimization-based method for simulating large multibody systems. *Optimization Methods & Software*, 24(6):871–894, 2009.
[26] Brian Sager and Dale Kaiser. Intercellular c-signaling and the traveling waves of myxococcus. *Genes & Development*, 8(23):2793–2804, 1994.
[27] Hale F Trotter. On the product of semi-groups of operators. *Proceedings of the American Mathematical Society*, 10(4):545–551, 1959.
[28] Katherine G Trudeau, Mandy J Ward, and David R Zusman. Identification and characterization of frzz, a novel response regulator necessary for swarming and fruiting-body formation in myxococcus xanthus. *Molecular microbiology*, 20(3):645–655, 1996.
[29] Takagi Tsutomu, Moritomi Yutaka, Iwata Jyun, and Nakamine Hiroshi. Mathematical model of fish schooling behaviour in a set-net. *Journal of Marine Science*, 61(7):1054–3139, 2004.
[30] Jorge Velázquez-Castro, Milica Lakovic, Esli Morales-Tehuitzitl, Inti A. Pagnuco, Carmen A. Ramírez, and Raul Costa-Pereira. A mathematical model of anarchy in bees. *Apidologie*, 51(6):1117–1124, 2020.
[31] Tamás Vicsek, András Czirók, Eshel Ben-Jacob, Inon Cohen, and Ofer Shochet. Novel type of phase transition in a system of self-driven particles. *Phys. Rev. Lett.*, 75(6):1226–1229, Aug 1995.
[32] Tamás Vicsek and Anna Zafeiris. Collective motion. *Physics Reports*, 517(3):71–140, 2012.
[33] Yong Zhang, Adrien Ducret, Joshua Shaevitz, and Tâm Mignot. From individual cell motility to collective behaviors: insights from a prokaryote, myxococcus xanthus. *FEMS microbiology reviews*, 36(1):149–164, 2012.